PAPER • OPEN ACCESS

SOLPS-ITER simulations of an X-point radiator in the ASDEX Upgrade tokamak

View the article online for updates and enhancements.

SOLPS-ITER simulations of an X-point radiator in the ASDEX Upgrade tokamak

O. Pan[1,*] , M. Bernert[1] , T. Lunt[1] , M. Cavedon[2] , B. Kurzan[1],
S. Wiesen[3] , M. Wischmeier[1], U. Stroth[1,4] and
the ASDEX Upgrade Team[a]

[1] Max-Planck-Institut für Plasmaphysik, 85748 Garching, Germany
[2] Dipartimento di Fisica 'G. Occhialini', Università di Milano-Bicocca, Milan, Italy
[3] Forschungszentrum Jülich Gmbh, Institut für Energie- und Klimaforschung-Plasmaphysik, 52425 Jülich, Germany
[4] Physik-Department E28, Technische Universität München, Garching, Germany

E-mail: ou.pan@ipp.mpg.de

CrossMark

Abstract

The X-point radiator (XPR) is an attractive scenario that may contribute to solving the power exhaust problem in future fusion devices. The 2D transport code SOLPS-ITER was applied to reproduce the experimentally measured plasma condition with an XPR in the ASDEX Upgrade tokamak and to compare with a reduced model. Neutrals penetrating from the adjoining cold divertor region and the large connection length near the X-point play an important role in initiating an XPR. However, once such a radiator is created, it persists even if the fueling and impurity seeding rates were reduced. The redistribution of plasma density and radiation near the X-point caused by fluid drifts at the XPR was studied in the simulation.

Keywords: X-point radiator, SOLPS-ITER, power exhaust

(Some figures may appear in colour only in the online journal)

1. Introduction

Power exhaust is one of the most critical issues for future fusion reactors, e.g. DEMO [1]. In order to guarantee the lifetime of the plasma-facing components, detached divertor conditions should be achieved to mitigate the power and particle fluxes reaching the divertor target [2–4]. In addition to this, transient events leading to heat pulses at the targets, e.g. from edge localized modes (ELMs), should also be suppressed. In experiments at metallic-wall tokamaks such as ASDEX Upgrade (AUG) and JET, a stable, localized and highly radiative phenomenon was observed near the X-point inside the confined plasma [5, 6]. This so-called X-point radiator (XPR)

can lead to a dissipated power fraction of 90%, mitigated ELMs and a fully detached divertor with a moderate confinement degradation [6], which is attractive for solving the power exhaust problem.

Recently, a series of experiments was carried out on AUG to study the operational window and the access condition of the XPR. The suppression of ELMs was achieved when the XPR was deep enough inside the confined region. The loss of ELMs was usually accompanied by a pressure degradation at the outboard mid-plane (OMP) [6]. The newly installed divertor Thomson scattering diagnostic in AUG is able to measure the electron density and temperature along its line of sight through the X-point region [7]. Significant lower temperatures and higher densities were observed at the X-point compared to the upstream position. A reduced model [8] was derived to explain the physical mechanisms for initiating a stable XPR by analysing the power balance between the upstream position and the XPR volume. A stable solution was found at a low X-point temperature (typically <5 eV with nitrogen as the main

---
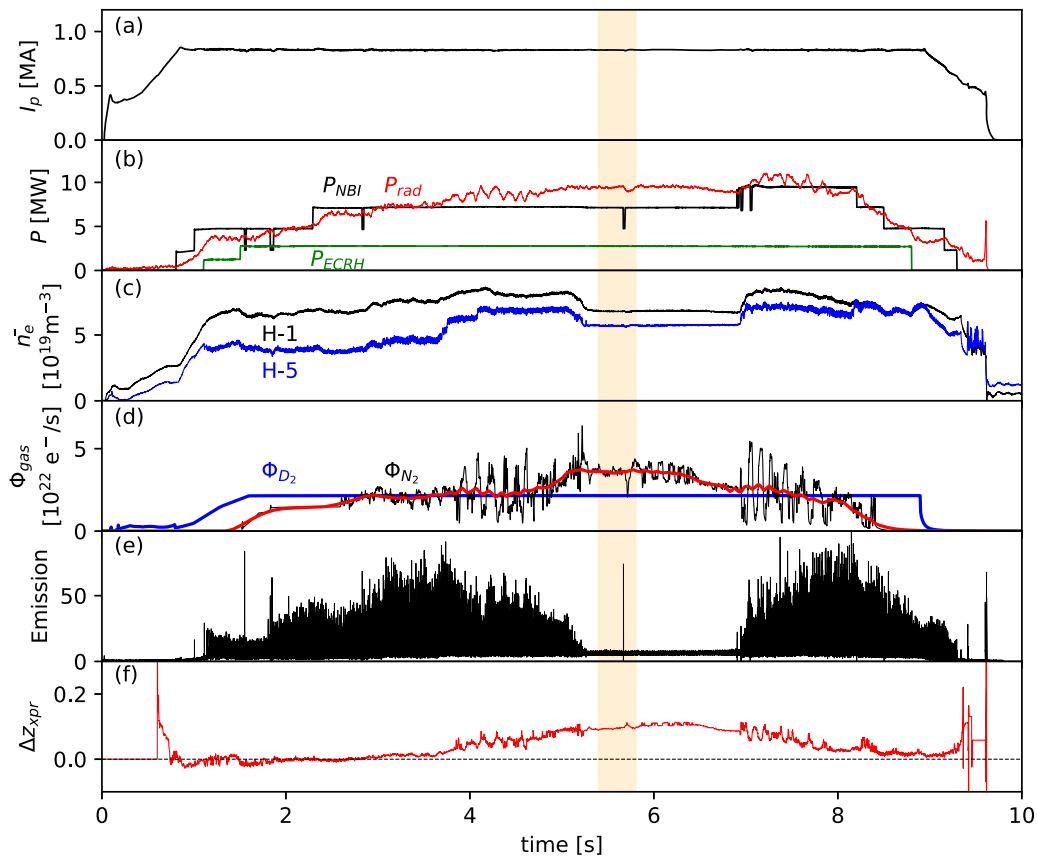
Figure 1. Time traces of (*a*) plasma current, (*b*) auxiliary heating power from NBI and ECRH and the total radiation power measured by bolometers, (*c*) line averaged electron density measured by interferometers along lines-of-sight through the core (H-1) and edge (H-5) plasma, (*d*) deuterium fueling rate in blue, raw and smoothed data of nitrogen seeding rate in black and red, respectively, (*e*) emission measured by the AXUV diagnostic to show the appearance of ELMs and (*f*) the vertical distance between the XPR and the X-point in AUG discharge #38773.

radiating impurity). In the reduced model, an access parameter was derived, $X_A \sim R_0^2 q_s^2 n_0 n_{e,u} f_{exp}/(a T_{e,u}^{2.5})$, that needs to be exceeded to establish an XPR, highlighting the role of the neutral density n_0, the safety factor q_s and the flux expansion f_{exp} at the X-point in the initiation of an XPR. This model reproduced experimental observations in AUG and shed light on the physical mechanism of the initiation and the stability of the XPR phenomenon. However, 2D numerical simulations are required to interpret the features not captured by the 0D reduced model, including the distribution of particle and power sources and sinks in the X-point region, the role of cross-field transport including drifts and the high-field-side/low-field-side asymmetry of an XPR.

In previous studies, the 2D transport code packages SOLPS5.0 [9] and SOLPS-ITER [10] have been improved to be able to reproduce the X-point radiating regime in a metallic device [11, 12], while a comparison with experimental measurements, especially with the newly installed divertor Thomson scattering and a comparison with the access condition in the reduced model are still missing. In this paper, the SOLPS-ITER code was applied to investigate the role of neutrals and the magnetic connection length in the initiation of an XPR, to depict the power and particle fluxes, sources and sinks inside the XPR region, as well as to reproduce the

experimental measurements in AUG by including the effect of drifts.

This paper is organized as follows: in section 2, the setup of the SOLPS-ITER simulation is introduced; in section 3, the initiation of an XPR is studied with simulations with a nitrogen seeding rate scan and compared with the reduced model; in section 4, a simple sketch of an XPR with a cold core is presented by analyzing the power and particle balances in detail; in section 5, various numerical experiments are carried out to study the role of neutrals in initiating and maintaining an XPR; in section 6, the SOLPS-ITER simulations with drifts activated are compared with the divertor Thomson scattering measurements, and the effect of drifts on the power and particle redistribution is discussed.

2. Simulation setup

The SOLPS-ITER code package, which consists of the multi-fluid transport code B2.5 [13] and the Monte Carlo code EIRENE [14] simulating the neutral particle transport, was applied in this work. The computational grids were generated on the magnetic equilibrium of AUG discharge #38773. The resolution of the grids is 120×36 in poloidal and radial directions, respectively. Compared to previous SOLPS simulations
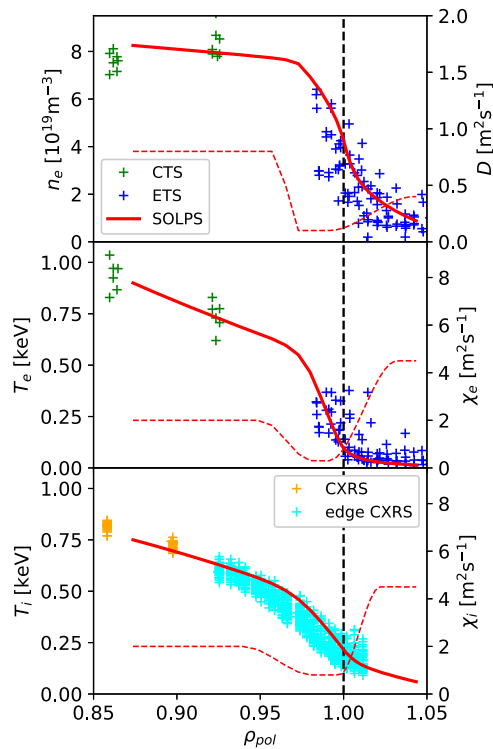
Figure 2. Radial profiles of electron density, electron temperature and ion temperature at the OMP, comparing the experimental measurements and the SOLPS-ITER modeling. The radial profiles of diffusive transport coefficients ($D_{\perp,i}$, $\chi_{\perp,e}$ and $\chi_{\perp,i}$) used in the simulation are shown by the dashed lines.

for AUG H-mode plasmas [15], a larger number of cells was set in poloidal direction to achieve a better resolution near the X-point. However, it should be noticed that, due to the constraint of quadrangle grids and the large flux expansion near the X-point, the resolution of the grids at the X-point cannot be as good as the one near the divertor targets. The typical global numerical residual is <2% for particles and <4% for power in the simulations in this paper. The developing version of SOLPS-ITER [16] with an extended grid structure may help to improve the resolution but this remains future work. The convergence criteria used in this work are based on those described in reference [10], including the steadiness of density, temperature, parallel velocity, potential and total recombination rate on a typical radial diffusion time scale (1 s).

In the simulations, deuterium and nitrogen were set as the main plasma and impurity species, respectively. The deuterium and nitrogen gases were puffed from the lower divertor private flux region, as in the experiments in AUG. The atomic and molecular reactions activated in the simulations include ionization, charge exchange, elastic collisions and volumetric recombination of deuterium atoms, ionization and volumetric recombination of nitrogen atoms and dissociation of deuterium and nitrogen molecule. Ammonia molecules were not included in this simulation. Charge exchange collisions between deuterium and nitrogen were found to contribute to the radiation in the pedestal region [17], while the reaction is still not included

in the SOLPS-ITER code manually. This is foreseen as future work.

In the simulations in sections 3–5, drifts and currents were switched off, and the sections focus on the general dependence of the initiation of an XPR on the plasma parameters at the upstream position and at the X-point, as well as the general features of particle and power balances inside the XPR. In section 6, $E \times B$ and diamagnetic drifts, as well as currents related to viscosity, ion-neutral friction and inertia were all fully activated in the simulations, in order to study the drift effects on the high-field-side/low-field-side asymmetry of an XPR and on the plasma potential and currents near the X-point.

3. Initiation of an XPR

In this section, the initiation of an XPR is studied by scanning the nitrogen seeding rate in the SOLPS-ITER simulations. The nitrogen seeding rate is also the commonly used controller in XPR experiments on AUG. The basic case of the simulations was set up based on the plasma condition in AUG discharge #38773 at 3.5 s. Figure 1 shows the time traces of the corresponding discharge parameters. The plasma current was 0.8 MA during the plateau. The toroidal field strength was $B = 1.8$ T and the ion gradient drift pointed to the X-point. From 2.5 s to 7 s, the neutral beam injection (NBI) and electron cyclotron resonance heating (ECRH) powers were 7.5 MW and 2.5 MW, respectively. While the deuterium fueling rate was kept constant at 2×10^{22} e$^-$ s^{-1}, the nitrogen seeding rate was feedback-controlled to achieve the preset position of the XPR. Figure 1(*f*) shows the vertical distance between the X-point and the highly radiative region measured by bolometers [6]. The radiator moved inside the confined region at about 3.5 s and then penetrated deeper with the increasing nitrogen seeding rate. As reported in reference [6], when the height of the XPR reached a certain value of about 10 cm above the magnetic X-point, ELM suppression was observed (see figure 1(*e*)).

The boundary conditions and radial transport coefficients in the basic case of the simulations were chosen to reproduce the plasma parameters of #38773 at 3.5 s. The innermost radial boundary of the grids was located at a normalized radius $\rho \approx 0.87$. The deuterium ion density, electron and ion temperatures at the innermost boundary were fixed according to the experimental values measured by the Thomson scattering (CTS, ETS) and charge exchange recombination spectroscopy (CXRS), resulting in an input power of 5.0 MW and 2.5 MW via the electron and ion channels, respectively. The particle recycling coefficient was set to 0.98 on the pumping surface behind the outer divertor target (see figure 3 in reference [15]) and 1.0 on other surfaces. For reproducing the experimental profiles, a deuterium gas fueling rate of 1×10^{22} e$^-$ s^{-1}, which is lower than the experimental value, was set in the simulation. Figure 2 shows the radial profiles of electron density, electron temperature and ion temperature at the OMP, as well as the radially varying particle and heat transport coefficients used in the simulation. The profiles in the simulation match the experimental measurements qualitatively.
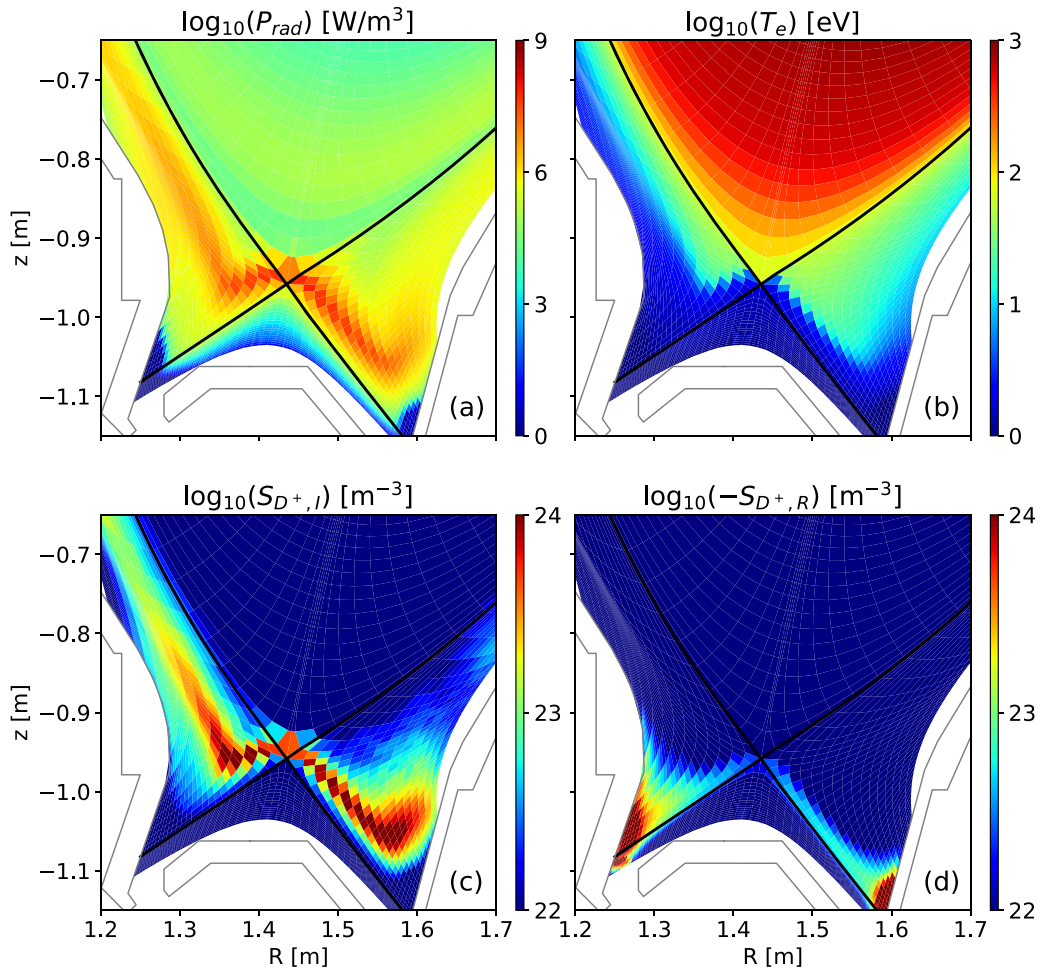
Figure 3. Cross sections of (*a*) line radiation density, (*b*) electron temperature, (*c*) deuterium ion source from ionization and (*d*) deuterium ion sink from volumetric recombination for $\Phi_N = 9.8 \times 10^{20}$ e$^-$ s^{-1}.

Similar to the experiments, the nitrogen seeding rate was scanned in the SOLPS-ITER simulations based on the basic case described in the previous paragraph. Figure 3 shows the cross sections of line radiation density, electron temperature, deuterium ion sources and sinks related to ionization and volumetric recombination for a nitrogen seeding rate of $\Phi_N = 9.8 \times 10^{20}$ e$^-$ s^{-1}, while figure 4 shows those for $\Phi_N = 2.1 \times 10^{21}$ e$^-$ s^{-1}. In the case with a lower nitrogen seeding rate, the temperature at the divertor targets is below 5 eV, indicating detached conditions, while the X-point region is still hot with a temperature of about 60 eV. The highly radiative and the ionizing regions are mainly located in the scrape-off layer (SOL) along the divertor legs. Volumetric recombination is found mainly in front of the divertor targets.

With the increasing nitrogen seeding rate in figure 4, the divertor region becomes colder and the highly radiative region moves towards the upstream position in the SOL and even penetrates inside the confined region near the X-point. The radiation and ionization are mainly concentrated in the confined region, surrounding a cold-core region with a temperature lower than 5 eV at the X-point with significant local volumetric recombination. It should be pointed out that the nitrogen seeding rate in the simulations was an order of magnitude lower

than the puffing rate in the experiments, while the nitrogen concentrations at the OMP in the simulations were similar to the experimental values (3%–4%). Such a phenomenon is commonly found in SOLPS-ITER simulations with impurity seeding. The reason may be related to 3D effects, molecular physics (e.g. ammonia production) and gas residence in pipes and hardware gaps, which is still an open question. When the nitrogen seeding rate exceeded 4×10^{21} e$^-$ s^{-1} in this simulation, a radiation collapse was found. Similar phenomena were reported in references [11, 12].

In reference [8], a reduced model was derived to explain the physical mechanisms for initiating a stable XPR. An XPR is generated when the access parameter,

$$X_A \sim R_0^2 q_s^2 n_{0,X} n_{e,u} f_{exp} / (a T_{e,u}^{2.5})$$
$$\sim n_{0,X} n_{e,u} f_{exp} B_{t,u}^2 / (T_{e,u}^{2.5} B_{\theta,u}^2), \tag{1}$$

exceeds a certain value. In equation (1), $n_{0,X}$ is the neutral density at the X-point, $n_{e,u}$ and $T_{e,u}$ are the electron density and temperature at the OMP, respectively, f_{exp} is the flux expansion between the OMP and the X-point, $B_{t,u}$ and $B_{\theta,u}$ are the toroidal and poloidal magnetic fields at the OMP, respectively.

The access parameter of the reduced model was checked in the SOLPS-ITER simulations. Figure 5 shows the evolution of
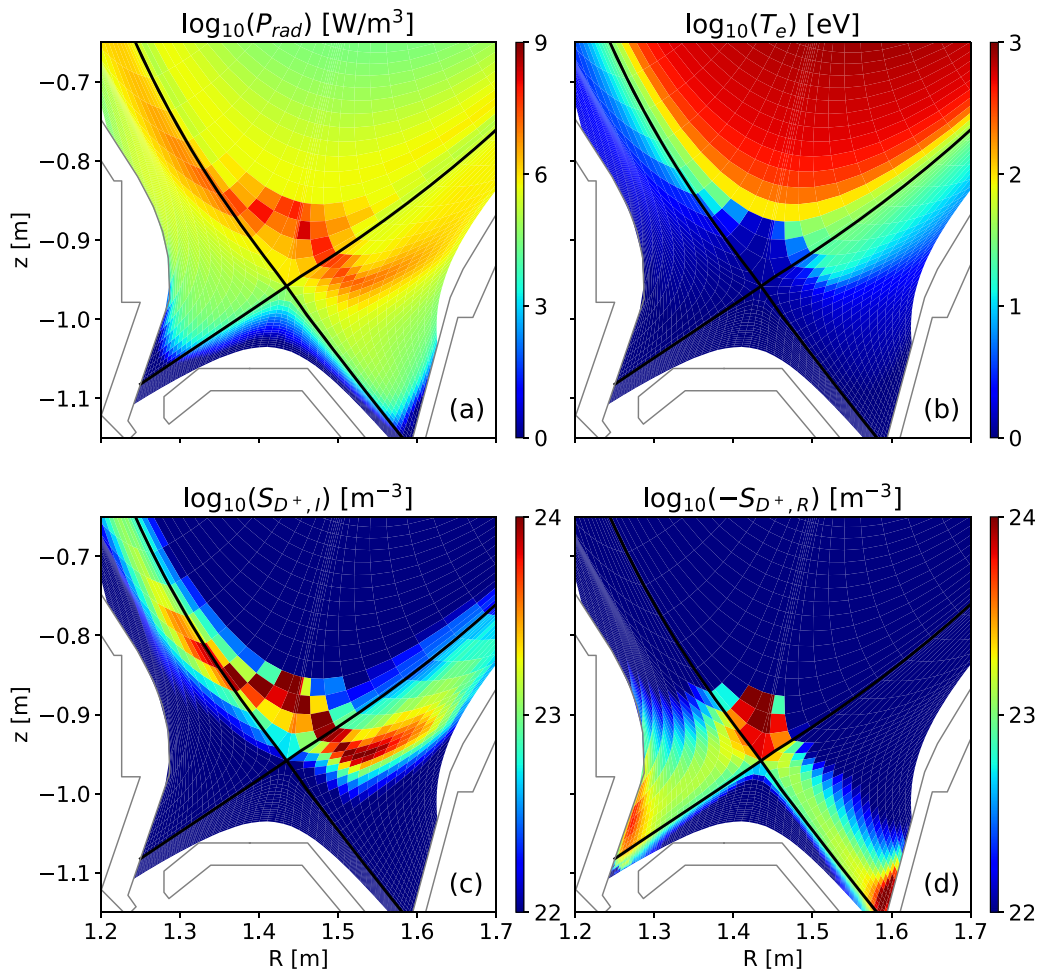
Figure 4. Same as figure 3 but for $\Phi_N = 2.1 \times 10^{21}$ e$^-$ s^{-1}.
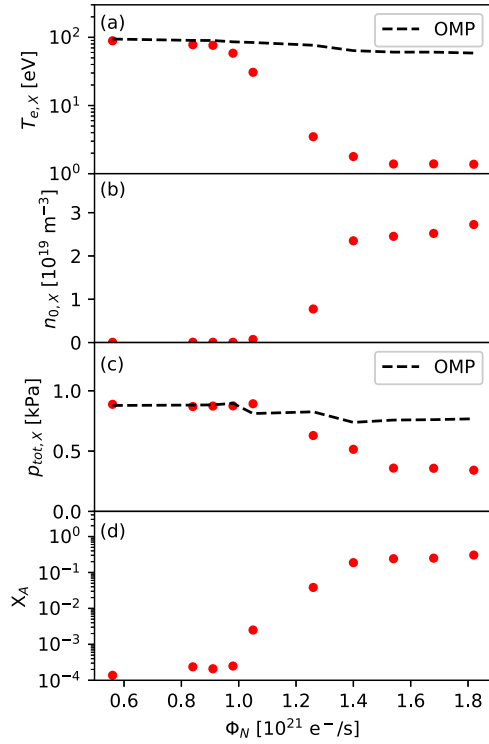
electron temperature, neutral density and total pressure at the X-point, as well as the X_A parameter defined by equation (1), in a scan of the nitrogen seeding rate. When the seeding rate is lower than 9.8×10^{20} e$^-$ s^{-1}, the neutral density at the X-point is low, and the electron temperature and the total pressure remain similar to those at the OMP. With the increasing nitrogen seeding rate, the divertor region and the PFR become colder and more transparent for the neutral particles which are recycled at the divertor targets or puffed by the gas valve. As a result, more neutrals are able to reach the X-point region and the neutral density at the X-point increases (see figure 5(*b*)). The atomic processes, e.g. ionization and charge exchange collision, of the neutrals further cool down the X-point region. When the nitrogen seeding rate exceeds 1.4×10^{21} e$^-$ s^{-1}, the electron temperature at the X-point drops below 5 eV, indicating the initiation of a cold XPR core. The neutral density at the X-point increases dramatically from about 5×10^{16} m^{-3} to about 2.5×10^{19} m^{-3}, giving the biggest contribution to the evolution of X_A. As a result, the X_A parameter increases with the increasing nitrogen seeding rate and saturates after the initiation of a cold XPR core.

When an XPR is generated, the electron temperature and the total pressure decrease both at the OMP and at the X-point (see figures 5(*a*) and (*c*)), while the decreases of temperature

and pressure at the X-point are stronger, resulting in a temperature and pressure gradient between the upstream position and the X-point. It is also worth noticing that the total pressure at the X-point exceeds the upstream value with $\Phi_N \approx 1.05 \times 10^{21}$ e$^-$ s^{-1}. The mechanism of the evolution of total pressure will be discussed in section 4 in detail.

Similar to figure 4(*b*) in reference [8], figure 6 shows the relation between the electron temperature at the X-point and the X_A parameter in the scan. The relation was checked in flux tubes at various normalized radii and shown by different colors. It is found that, for all flux tubes shown here, an XPR with a cold core ($T_{e,X} < 5$ eV) only occurs when the value of X_A exceed a certain threshold. In addition to this, the threshold values are similar for the flux tubes at different radii.

According to equation (1), an XPR can be achieved with a smaller magnetic pitch angle ($\sin a \approx B_{\theta,u}/B_{t,u}$) and a larger flux expansion at the X-point. This is because the larger connection length and flux expansion can lead to a larger volume for volumetric processes at the X-point and lower parallel heat flux density reaching the X-point region. In order to check the effect of the magnetic pitch angle, a similar nitrogen seeding rate scan was carried out in simulations with a toroidal magnetic field of 2.5 T. Comparing the simulations with the same input parameters but different toroidal magnetic fields,

Figure 5. Evolution of (*a*) electron temperature, (*b*) neutral density and (*c*) total plasma pressure at the X-point with a scan of the nitrogen seeding rate. The electron temperature and total plasma pressure at the OMP are also shown in (*a*) and (*c*) by dashed lines for comparison. The X_A parameter calculated by equation (1) is shown in (*d*).
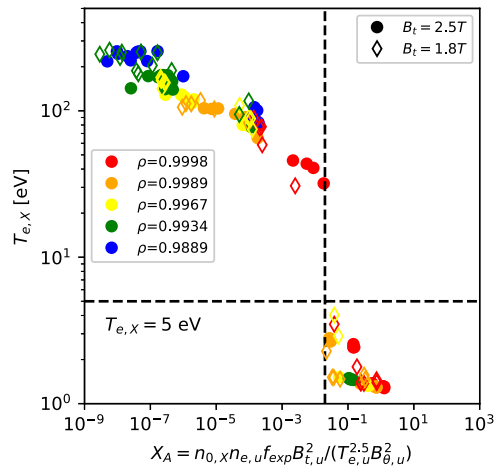
Figure 6. Variation of the electron temperature near the X-point with the X_A parameter in the flux tubes at various normalized radii. The cases with a toroidal field of 1.8 T are marked by diamond points and those with 2.5 T by dot points.

the case with a toroidal field of 2.5 T (i.e. with a larger connection length) shows an XPR deeper inside the confined region compared to the case with 1.8 T. The $T_{e,X}-X_A$ relation in the simulations with 2.5 T is also plotted in figure 6 with dot symbols. It is found that the threshold of X_A is robust with different toroidal field strengths. This indicates that the XPR access condition derived in the reduced model conclusively contains the main features related to the magnetic field.
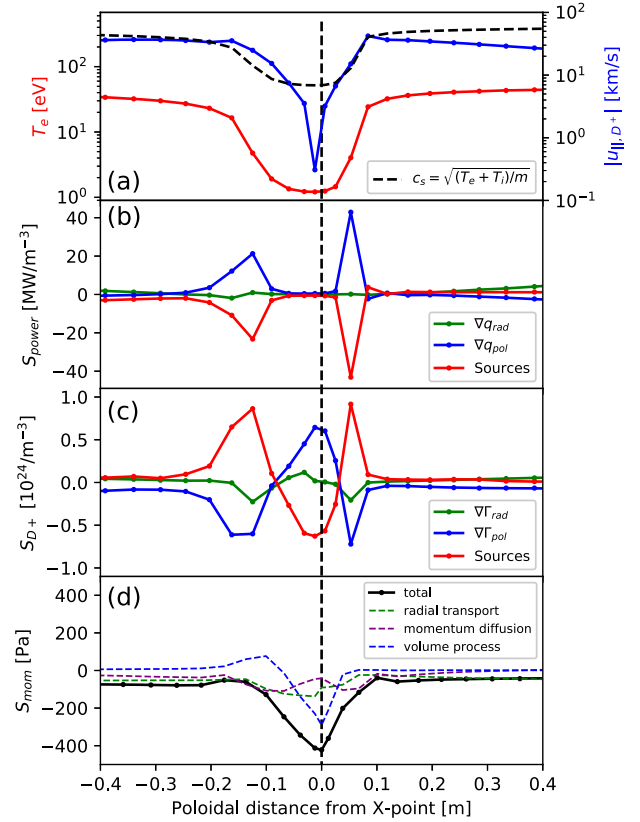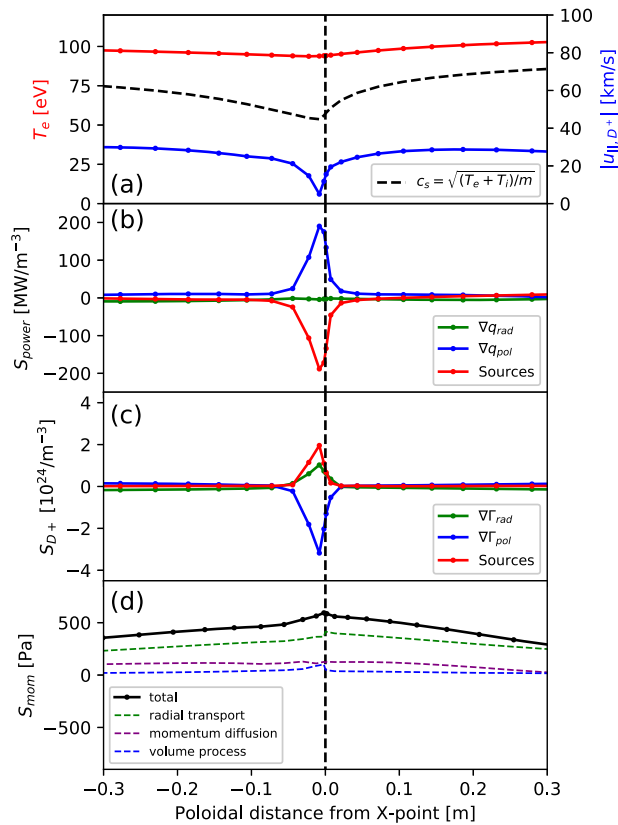

Figure 7. The poloidal profile of (*a*) the electron temperature and the parallel velocity of deuterium ions, the balance of (*b*) power, (*c*) particle and (*d*) pressure in a flux tube through the cold XPR core.

In reference [18], it was also found that an XPR was achieved in the snowflake divertor configuration with a much lower nitrogen seeding rate than that in the conventional single-null configuration, benefiting from the dramatically larger connection length and flux expansion near the X-point in the snowflake configuration.
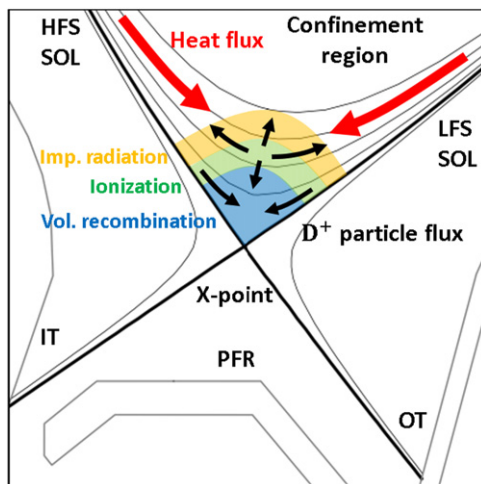
4. Power and particle balances of an XPR with a cold core

With the existence of a cold XPR core, as shown in figure 4, there are large poloidal temperature gradients and large particle sources/sinks in the region near the X-point, which can also lead to strong heat and particle transport. It is important to analyze the power and particle balances at an XPR in order to get physical insight of this phenomenon. The SOLPS-ITER simulations can provide such an insight with a steady-state fluid picture coupled with neutral physics. That a fluid picture works well for the XPR may be because the plasma at the X-point is cold, dense and with a high collisionality, i.e. suitable for the fluid assumptions. However, in the future, other numerical codes may be applied to study the transient features of the XPR with a view on MHD stability and turbulence.

Figure 7 shows the poloidal profiles of the electron temperature and the absolute value of parallel ion fluid velocity, as well as the power, particle and momentum sources/sinks along the flux tube through the cold XPR core. The XPR

Figure 8. The same as in figure 7 but in a flux tube at the innermost radial boundary of the XPR.

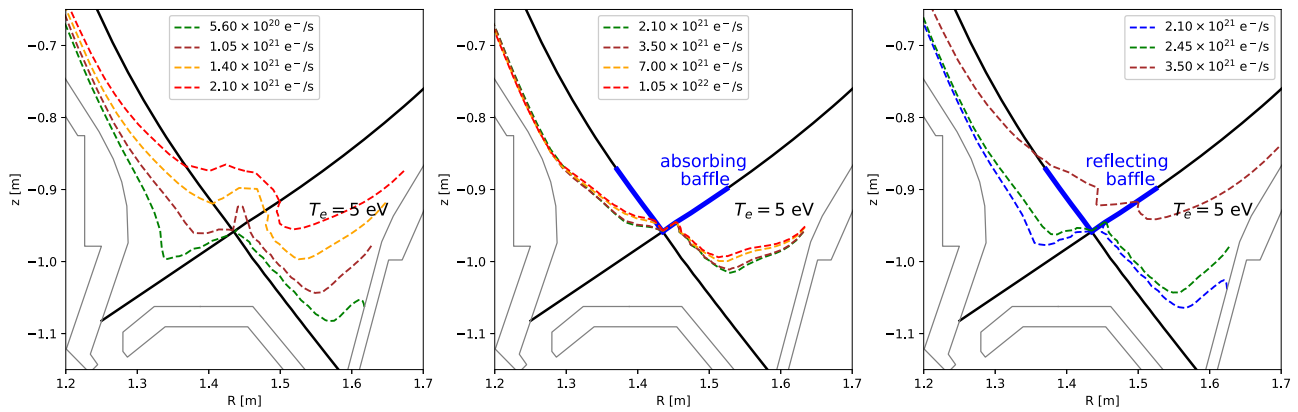**Figure 9.** A simple sketch of an XPR with a cold core.

by impurity radiation. At the edge of the XPR, maximum and minimum are found in the divergence of the poloidal heat flux and the volume power sink, respectively, indicating that the power from the inner confined region is transported poloidally to the XPR region and dissipated by radiation at the edge of the XPR. In the highly radiative region (see the well regions in the red curve in figure 7(*b*)), the temperature decreases sharply. In the cold XPR core at the X-point, the temperature decreases to a value of about 1 eV, and the radiation becomes small due to the low temperature. In figure 7(*c*), the green and blue curves show the divergence of the radial and poloidal D^+ particle flux, respectively, while the red curve shows the D^+ particle source/sink including ionization and volumetric recombination. At the edge of the cold XPR core with a temperature of about 10 eV, a band with a high deuterium ionization source is found (see the peak regions in the red curve in figure 7(*c*)), surrounding the cold XPR core with a strong volumetric recombination sink (see the well region in the red curve). As shown by the blue curve in figure 7(*c*), poloidal particle fluxes are generated from the ionizing region to the recombining zone, dominated by convective transport. The parallel ion fluid velocity is close to the local sound speed in the ionizing region, while decreasing significantly in the recombining region (see figure 7(*a*)). A small divergence of radial particle flux is found in the green curve in the ionizing zone, mostly caused by the diffusive particle fluxes directed radially outward. Figure 7(*d*) shows the momentum source integrated from the OMP to the X-point. At the upstream position, the total plasma pressure keeps nearly constant in the flux tube. In the ionizing region, the parallel velocity increases and leads to an increase in the dynamic pressure, resulting in a slight increase of the total pressure at the edge of the cold XPR core. In the cold XPR core region, with charge exchange and volumetric recombination setting in, as well as the cross-field transport and the momentum diffusion, a substantial pressure loss is found, as shown by the well in the black curve in figure 7(*d*).

Figure 8 shows the poloidal profiles along the flux tube at the innermost radial boundary of the cold XPR core. A small poloidal temperature gradient is found in figure 8(*a*), leading to a conductive heat flux from the upstream position to the X-point region. Most of the power is dissipated at the X-point by radiation, as shown by the large power sink in the red curve in figure 8(*b*). At the X-point, the strong local ionization and the particle flux radially from the outer highly ionizing region contribute to the particle sources in figure 8(*c*) and increase the plasma total pressure near the X-point. The pressure gradient in figure 8(*d*), in consequence, leads to poloidal particle fluxes leaving the X-point region towards the upstream position. The convective heat flux carried by the particle flux partly compensates for the conductive heat flux from the upstream position, while the conductive heat transport is still dominant. The balances at the boundary of the XPR region indicate that the large particle source in the cold XPR core is important for the XPR to move further inside the confined region.

With the power, particle and momentum balances, a simple sketch of an XPR with a cold core can be depicted, as shown in figure 9. With impurity seeding, the divertor region is cooled

is located in the region with a poloidal distance from the X-point $-0.2 < d_{\mathrm{pol},x} < 0.1$ m. Outside the XPR region, the electron temperature shows a small gradient from the upstream position to the boundary of the XPR. Since the conductive heat transport is given by $q_{\mathrm{cond}} = \kappa T_{\mathrm{e}}^{5/2} \nabla T_{\mathrm{e}}$, a small parallel temperature gradient is enough to lead to a large parallel heat flux. In figure 7(*b*), the green and blue curves show the divergence of the radial and poloidal heat flux, respectively, while the red curve shows the volume power sink dominated

Figure 10. Contour of $T_e = 5$ eV in a scan of the nitrogen seeding rate (*a*) without neutral baffles, (*b*) with an absorbing baffle and (*c*) with a reflecting baffle to hinder neutral penetrating the confined region.

Table 1. Deuterium neutral sources relating to the ionization in the confined region ($S_{i,core}$) and in the SOL and the PFR ($S_{i,SOL+PFR}$), relating to the particle recycling from the divertor target and chamber wall (S_{recyl}) and relating to the volumetric recombination in the confined region ($S_{recom,core}$) and in the SOL and the PFR ($S_{recom,SOL+PFR}$), compared between cases with/without an XPR and with/without volumetric recombination (VRC).

Particle source $(10^{23}$ s$^{-1})$	Without XPR (with VRC)	With XPR (with VRC)	With XPR (without VRC)
$S_{i,core}$	−0.11	−0.66	−0.18
$S_{i,SOL+PFR}$	−1.34	−0.78	−0.71
S_{recyl}	0.97	0.47	0.89
$S_{recom,core}$	<0.01	0.50	0.0
$S_{recom,SOL+PFR}$	0.48	0.46	0.0

down by impurity radiation. When the temperature in the divertor is low, impurity particles penetrate the confined region near the X-point and reduce the temperature there via line radiation. The large flux expansion and large connection length in the vicinity of the X-point promote the volumetric processes. The parallel temperature gradient leads to a parallel conductive heat flux from the upstream position to the X-point in a narrow layer inside the separatrix. The SOL and divertor receive less power and become even colder, which decreases the opacity for neutrals. More neutrals are able to reach the X-point region and ionized there. Plasma density and pressure increase in the highly ionizing zone, leading to a radially inward diffusion and a parallel convective particle flux from the ionizing zone to the upstream position. The temperature at the X-point is reduced further by the deuterium ionization losses, and the cold core region of the XPR expands further into the confined region. When the temperature at the X-point reaches around 1 eV, the volumetric recombination rate increases substantially. Plasma pressure drops in the cold XPR core due to volumetric processes, momentum diffusion and radial transport, resulting in a parallel convective particle flux from the ionizing zone to the recombining zone. The particle recycling from the divertor and main chamber wall decreases, while the total ionization rate keeps almost constant, mainly supplied by neutrals generated by volumetric recombination.

5. Maintenance of an XPR with a cold core

The SOLPS-ITER simulations and the reduced model both indicate that neutrals in the X-point region play an important role in the initiation of an XPR. In order to test the effect of neutrals, numerical experiments were carried out by setting a virtual baffle near the X-point in the simulation acting on the neutral particles only, which hinders neutrals penetrating the confined region from the SOL and the PFR near the X-point, as shown in figure 10. Such a baffle cannot exist in experiments. Two types of baffles were tested. In the case shown in figure 10(*b*), the baffle was set to absorb all neutrals impinging from the SOL and the PFR. Other input parameters were kept the same as the case with an XPR shown in figure 10(*a*) with $\Phi_N \approx 2.1 \times 10^{21}$ e$^-$ s^{-1}. In the case with an absorbing baffle, the highly radiative region located at the X-point, and the ionization and volumetric recombination rates stayed very low in the confined region. As shown by the temperature contours, no cold XPR core was found. Even when the nitrogen seeding rate was increased by a factor of 5, the radiative and low-temperature region did not move further inside, and the ionization and volumetric recombination reactions remained weak in the confined region. This means that without the neutrals penetrating the confined region near the X-point, an XPR with a cold core is not achievable. In the case shown in figure 10(*c*), the baffle reflects neutrals reaching the side facing the SOL and the PFR. Starting with a case without an XPR, the low-temperature region cannot move inside the confined region until the low-temperature region in the high-field-side SOL expanded beyond the edge of the baffle so that the neutrals could enter the confined region bypassing the baffle (see the case with $\Phi_N \approx 3.5 \times 10^{21}$ e$^-$ s^{-1} in figure 10(*c*)). This indicates that neutrals that fly from the SOL and the PFR into the confined region near the X-point are essential for the inward movement of the low-temperature region and the initiation of an XPR with a cold core.

As discussed in reference [8], these neutrals play an important role in the initiation of an XPR, while they are not essential for maintaining it. Similar results were found in the SOLPS-ITER simulations. Starting with a case with an
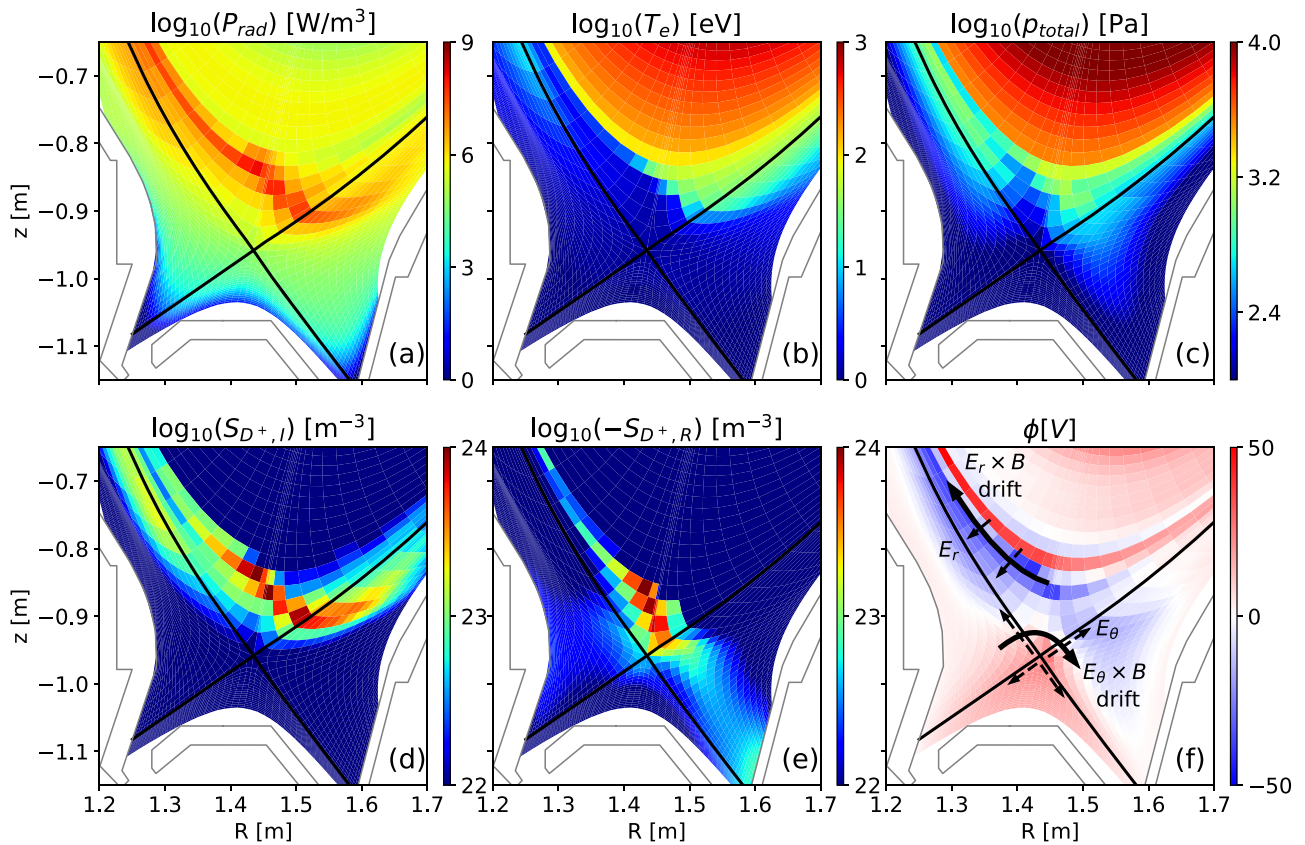
Figure 11. Cross sections of (*a*) line radiation density, (*b*) electron temperature, (*c*) total pressure, (*d*) deuterium ionization rate, (*e*) deuterium volumetric recombination rate and (*f*) plasma potential in the simulation with drifts with $\Phi_N = 2.1 \times 10^{21}$ e$^-$ s^{-1}.

XPR and decreasing the deuterium puffing rate, the XPR survived although the fueling rate was reduced by an order of magnitude.

As mentioned in section 4, the high ionization rate in the XPR region is mainly supplied by the local volumetric recombination. However, once the XPR is created, it persisted even when the volumetric recombination reaction was switched off in the simulation. Table 1 compares the deuterium neutral sources in the cases with and without volumetric recombination. Without volumetric recombination, the ionization rate decreased and was fully supplied by the recycling neutrals from the divertor and main chamber wall. The volumetric recombination was not essential for maintaining the XPR, however, as shown in the previous section, the strong volumetric recombination supplies the strong ionization which leads to the high density and the inward diffusion in radial direction, which is important for the expansion of the XPR further into the confined region. Meanwhile, it is still an open question whether the wall recycling can supply an XPR in a larger device where the wall is further away from the X-point.

The maintenance of the XPR was also tested by reducing the nitrogen seeding rate in the simulation. The XPR remained even when the nitrogen seeding rate was reduced by a factor of 5, which is much lower than the threshold found in the scan from a low seeding rate to a high seeding rate. However, the XPR vanished when the seeding rate was too low since a

certain amount of impurities was necessary for dissipating the power reaching the X-point volume.

6. Poloidal asymmetry and the effects of drifts

Drifts were found to influence the high-field-side/low-field-side asymmetry of divertor plasma conditions in experiments and numerical simulations [11, 19–24]. In the previous sections, it was shown that there are significant ionization and volumetric recombination in the region with an XPR. This can lead to large gradients of plasma potential and pressure near the X-point, which, in consequence, can drive $E \times B$ and diamagnetic flows. These are discussed in the following.
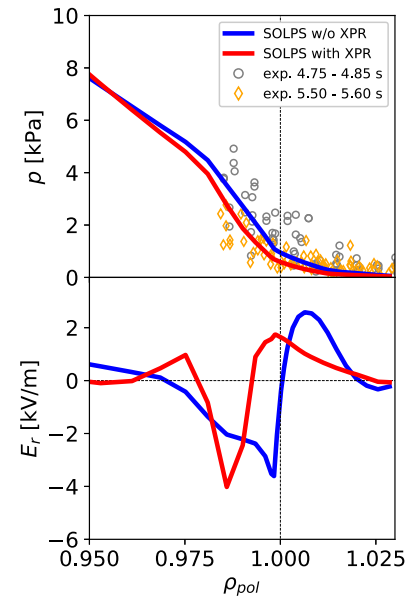
Applying similar settings as in reference [25] to avoid the numerical instabilities and accelerate the computation, $E \times B$ and diamagnetic drifts, as well as currents related to viscosity compensation, ion-neutral friction and inertia were activated in the SOLPS-ITER simulations with an XPR. Figure 11 shows resulting poloidal distributions of line radiation density, electron temperature, total pressure, deuterium ion sources/sinks related to ionization and volumetric recombination, as well as the plasma potential. The toroidal magnetic field points out of the paper and therefore $B \times \nabla B$ points downwards. Compared to the simulations without drifts in section 3, the cold and dense core of the XPR expands towards the upstream position on the high-field side. In the highly ionizing region, a low plasma potential was found, corresponding to the Boltzmann
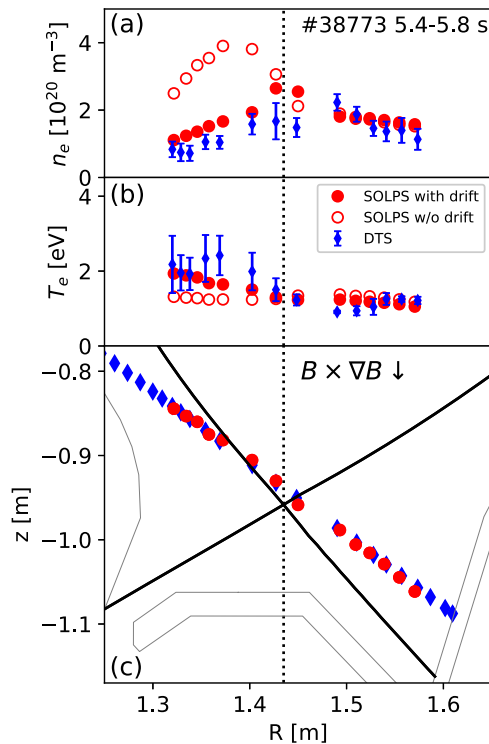
Figure 12. Electron density and temperature measured by the divertor Thomson scattering diagnostic (DTN) along its line of sight and in the SOLPS-ITER simulations with and without drifts. The nitrogen seeding rate was 2.1×10^{21} e$^-$ s^{-1} in both cases. The divertor Thomson scattering data was taken in the time phase with an significant XPR in #38773, as shown by the orange area in figure 1.

Figure 13. Radial profiles of the plasma pressure and the radial electric field at the OMP, comparing simulations with $\Phi_N = 1.54 \times 10^{21}$ e$^-$ s^{-1} (without an XPR with a cold core) and $\Phi_N = 2.10 \times 10^{21}$ e$^-$ s^{-1} (with an XPR with a cold core). The experimental pressure values estimated by $(T_e + T_i)n_e$ before (4.75–4.85 s, $\Phi_N \approx 2.6 \times 10^{22}$ e$^-$ s^{-1}) and during (5.50–5.60 s, $\Phi_N \approx 3.5 \times 10^{22}$ e$^-$ s^{-1}) an XPR with a cold core are also plotted for information, where T_e and n_e were measured by the edge Thomson scattering and T_i by the edge CXRS.

factor. Radial electric fields were generated by the potential gradients, pointing from the inner confined region to the highly ionizing region, resulting in $E_r \times B$ drifts from the X-point to the high-field-side upstream position. A potential hill was found at the X-point, which corresponds to the poloidal current leaving the X-point to the divertor targets and to the upstream position [26]. Given the temperature and its gradient as well as the electric conductivity near the X-point were already low, the currents were mainly driven by the poloidal electric field. The poloidal electric field pointing away from the X-point led to an $E_\theta \times B$ drift transporting particles clockwise from the high-field-side SOL to the low-field-side SOL above the X-point. As discussed in section 4, a pressure drop was found in the cold XPR core. This led to a diamagnetic drift surrounding the cold XPR core from the X-point to the high-field-side upstream position. The drifts influenced the particle and power distribution near the X-point region. The plasma density in the high-field-side SOL decreased, while the cold and dense region of the XPR expanded towards the upstream position in the high-field-side confined region.

The drift effects were found to contribute to a better agreement between the simulation and the experimental measurements. Figures 12(*a*) and (*b*) shows the electron density and temperature along the measuring line-of-sight of the divertor Thomson scattering diagnostic, comparing the experimental data and the SOLPS-ITER simulations with and without drifts. Compared to the case without drifts, the case

with drifts showed lower electron densities and higher electron temperatures in the high-field-side SOL, matching better the experimental measurements.

In addition to this, the upstream radial electric field was also found to be influenced by the existence of the XPR. In figure 13, compared to a case with the same transport coefficients but with a reduced nitrogen seeding rate and without an XPR, the E_r shear layer shifted further inside in the case with an XPR. Similar results were also found in reference [27]. Correspondingly, in the radial profile of pressure at the OMP, the large-gradient region also moved inside and the pressure at the separatrix decreased. The change in the pressure is also consistent with the experimental findings qualitatively [6] and may contribute to explaining the suppression of ELMs in the experiment with an XPR.

7. Conclusion and outlook

The SOLPS-ITER code package has been applied to study the XPR phenomenon in the ASDEX Upgrade tokamak. The two-dimensional simulations showed qualitative agreement with the experimental measurements and a reduced model for an XPR, filling in the gaps between the experiments and theoretical analysis. The particle, power and momentum balances in the region with an XPR were analysed. In the flux tube close to the separatrix, a cold XPR core was discovered with recombining region at an electron temperature of $\sim$1 eV. The cold XPR core is surrounded by bands of ionizing and radiating regions with an electron temperature of $\sim$10 eV.

Most of the power from the upstream position is dissipated in the radiating and ionizing region where a large poloidal temperature gradient is found. Convection appears to transport particles from the ionizing region to the recombining region. The parallel ion velocity is close to the local sound speed in the ionizing region, while decreasing significantly in the recombining region. Momentum loss was found in the cold XPR core, caused by volumetric processes, cross-field transport and momentum diffusion.

The simulation results were compared with the reduced model for an XPR. By checking the dependence between the X-point temperature and the X_A parameter in simulations with a nitrogen seeding rate scan, a threshold of the X_A parameter was found for the initiation of an XPR with a temperature below 5 eV. The threshold is robust for different flux tubes at various radii and for different toroidal magnetic field strengths, indicating that the reduced model already contains the most important physics for initiating an XPR.

The activation of drifts and currents ($B \times \nabla B$ points to the primary X-point) in the simulation improved the agreement with the experimental measurements by the divertor Thomson scattering diagnostic, especially on the high-field side. A lower electron density was found in the case with drifts in the high-field-side SOL near the separatrix, the radial and poloidal $E \times B$ drift may play an important role in such a redistribution of particles. In addition to that, the low plasma potential in the ionizing region of the XPR was also found to influence the upstream condition. The shear layer of the radial electric field shifted inward in the case with an XPR compared to that without an XPR, which also relates to the shift of the plasma pressure profile at the OMP.

Impurity transport at the XPR, comparison of XPRs with different impurities, e.g. Ne and Ar, as well as the scaling law in devices with different sizes, are foreseen as future work.

Acknowledgments

ORCID iDs

O. Pan ⬤ https://orcid.org/0000-0003-3827-0674
T. Lunt ⬤ https://orcid.org/0000-0002-7386-1456
M. Cavedon ⬤ https://orcid.org/0000-0002-0013-9753
S. Wiesen ⬤ https://orcid.org/0000-0002-3696-5475
U. Stroth ⬤ https://orcid.org/0000-0003-1104-2233

References

[1] Zohm H. *et al* 2013 *Nucl. Fusion* **53** 073019
[2] Wenninger R. *et al* 2016 *Nucl. Fusion* **57** 016011
[3] Wenninger R. *et al* 2014 *Nucl. Fusion* **54** 114003
[4] Wischmeier M. *et al* 2015 *J. Nucl. Mater.* **463** 22
[5] Bernert M. *et al* 2017 *Nucl. Mater. Energy* **12** 111
[6] Bernert M. *et al* 2021 *Nucl. Fusion* **61** 024001
[7] Kurzan B., Lohs A., Sellmair G. and Sochor M. 2021 *J. Instum.* **16** C09012
[8] Stroth U. *et al* 2022 *Nucl. Fusion* **62** 076008
[9] Schneider R. *et al* 2006 *Contrib. Plasma Phys.* **46** 3
[10] Wiesen S. *et al* 2015 *J. Nucl. Mater.* **463** 480
[11] Reimold F. *et al* 2015 *J. Nucl. Mater.* **463** 128
[12] Senichenkov I., Kaveeva E.G., Rozhansky V.A., Voskoboynikov S.P., Veselova I.Y., Shtyrkhunov N.V., Coster D.P. and Bonnin X. 2021 *Plasma Phys. Control. Fusion* **63** 055011
[13] Braams B.J. *et al* 1987 *NET-Report 142/83-11/FU-NL/NET* Plasma Physics Laboratory, Princeton University (http://www.eirene.de/Braams-NET-report.pdf) (Princeton, USA)
[14] Reiter D., Baelmans M. and Börner P. 2005 *Fusion Sci. Technol.* **47** 172–186
[15] Chankin A.V. *et al* 2006 *Plasma Phys. Control. Fusion* **48** 839
[16] Dekeyser W. *et al* 2021 *Nucl. Mater. Energy* **27** 100999
[17] Dux R., Cavedon M., Kallenbach A., McDermott R.M. and Vogel G. (the ASDEX Upgrade Team) 2020 *Nucl. Fusion* **60** 126039
[18] Pan O. 2020 *PhD Thesis* Technical University of Munich
[19] Potzel S. *et al* 2015 *Nucl. Fusion* **54** 013001
[20] Jaervinen A.E. *et al* 2017 *Nucl. Mater. Energy* **12** 1136
[21] Jaervinen A.E. *et al* 2019 *Nucl. Mater. Energy* **19** 230
[22] Rozhansky V. *et al* 2018 *Contrib. Plasma Phys.* **58** 540
[23] Senichenkov I. *et al* 2022 *Contrib. Plasma Phys.* **62** e202100177
[24] Wensing M., Loizu J., Reimerdes H., Duval B.P. and Wischmeier M. (the TCV team) 2020 *Nucl. Fusion* **60** 054005
[25] Rozhansky V., Molchanov P., Veselova I., Voskoboynikov S., Kirk A. and Coster D. 2012 *Nucl. Fusion* **52** 103017
[26] Rozhansky V., Kaveeva E., Senichenkov I., Sorokina D., Vekshina E., Coster D., McCarthy P. and Khromov N. 2021 *Plasma Phys. Control. Fusion* **63** 015012
[27] Senichenkov I., Kaveeva E., Rozhansky V. and Coster D. 2021 *Phys. Plasmas* **28** 062507